Ceramics International 50 (2024) 2350–2362

Contents lists available at ScienceDirect

Ceramics International

journal homepage: www.elsevier.com/locate/ceramint

Critical roles of multiphase coexistence in boosting piezo-catalytic activity of $BaTiO_3$-based piezoelectric ceramics

Daen Zhao [a], Yongbo Gao [a], Luoping Yang [a], Yanhong Chen [a], Yuesha Wang [a], Qiaoji Zheng [a], Kwok-Ho Lam [b,*], Dunmin Lin [a,**]

[a] College of Chemistry and Materials Science, Sichuan Normal University, Chengdu, 610066, China
[b] Centre for Medical and Industrial Ultrasonics, James Watt School of Engineering, University of Glasgow, Glasgow, Scotland, UK

ARTICLE INFO

Handling Editor: Dr P. Vincenzini

Keywords:
$BaTiO_3$
Phase structure
Multiphase coexistence
Electrical properties
Catalytic performance

ABSTRACT

Recently, piezocatalysis induced by perovskite ferroelectric ceramics has widely been favored as a possible fascinating strategy for water remediation due to its low cost, simplicity and feasibility. Herein, a strategy of three-ferroelectric-phase coexistence is proposed to boost the piezocatalytic performance of $BaTiO_3$-based ceramics by introducing $Ca(Sn_{0.5}Zr_{0.5})O_3$ into $BaTiO_3$. The piezocatalysts of $(1\text{-}x)BaTiO_3$–$xCa(Sn_{0.5}Zr_{0.5})O_3$ ceramics were prepared by a high-temperature solid-phase method. The phase structure, microstructure, electrical properties and catalytic performance of ceramics were comprehensively studied. As x increases from 0 to 0.10, the ceramics undergo the phase evolution from single tetragonal phase to multiphase (coexistence of rhombic, orthorhombic, and tetragonal phases). It is found that the phase structure of the ceramics plays a critical role in enhancing the piezocatalytic activity. The pure $BaTiO_3$ exhibits the tetragonal (T) phase with few spontaneous polarization directions and high polarization rotational energy barrier, resulting in poor catalytic performance and low piezoelectricity. With the coexistence of rhombic (R), orthorhombic (O) and tetragonal (T) phases, the ceramic with $x = 0.1$ exhibits the increased spontaneous polarization directions and low polarization rotational energy barrier, leading to excellent catalytic performance and high piezoelectricity. Especially, for the ceramics with $x = 0.10$, the degradation rates of rhodamine B (RhB), methylene blue (MB) and methyl orange (MO) under ultrasonication reach 97 %, 93 % and 73 %, respectively. In addition, the influencing factors of piezocatalytic degradation of RhB and the catalytic mechanism are investigated. This work proposes an environmentally friendly piezoelectric material for improving the water environment and a strategy for improving the catalytic activity of $BaTiO_3$-based lead-free piezoelectric materials.

1. Introduction

With the rapid economic growth, the industrialization process is significantly promoted, accompanying with accelerated release of various industrial dyes into water. It is well known that the dyes are difficult to be decolorized or degraded due to their complex composition, deep coloration and high organic content, resulting in severe environmental pollution and health problems [1–4]. Hence, it is urgent to develop efficient, environmentally friendly, and renewable methods for water remediation. In the past decades, photocatalysis has been proven as promising degradation technology owning to unique electronic and optical properties of photocatalysts [5–7]. Nevertheless, the conversion efficiency of photocatalysts heavily depends on the light absorption efficiency, and photoexcited electron-hole pair separation and recombination [8], which limits their applications in real-life. Although various strategies, such as morphology and size control [9], heterojunction coupling [10], and noble metal modification [11], have been developed to promote the separation of photoexcited electron-hole pair, the sophisticated fabrication process and high cost of photocatalysts still restrict their practical applications. Accordingly, the development of novel progressive catalysts and catalytic techniques with improved efficiency is an imperative and challenging task for environment purification.

Piezoelectric materials can convert mechanical energy into electrical energy, which have been utilized extensively in some advanced sensors, transducers, and electronic devices [12–14]. It has been reported that

* Corresponding author.
** Corresponding author.
E-mail addresses: kwokho.lam@glasgow.ac.uk (K.-H. Lam), ddmd222@sicnu.edu.cn (D. Lin).

https://doi.org/10.1016/j.ceramint.2023.11.013
Received 24 June 2023; Received in revised form 18 August 2023; Accepted 1 November 2023
Available online 2 November 2023
0272-8842/© 2023 The Authors. Published by Elsevier Ltd. This is an open access article under the CC BY license (http://creativecommons.org/licenses/by/4.0/).

the piezoelectric materials generate polarized charges under external mechanical stress and create a built-in electric field, modifying the energy band structure and facilitating the separation and migration of charges and holes [15]. Piezocatalysis has been successfully applied to degradation of organic pollutants [16–18], absorption of CO_2 [19,20], production of hydrogen [21,22] and applied medicine [23,24]. For instance, Zhang et al. synthesized a rectangular shaped $Na_{0.5}Bi_{0.5}TiO_3$ (BNT) piezoelectric micron crystal by a hydrothermal method with 59 % degradation of rhodamine B (RhB) in 180 min under ultrasonication [18]. Zhang et al. designed Nb-doped $Pb_{0.99}(Zr_{0.95}Ti_{0.05})_{0.98}Nb_{0.02}O_3$ (PZTN) piezoelectric particles, in which the spontaneous polarization of PZTN is changed dramatically to generate positive and negative charges, leading to a reduction of CO_2 by 789 mmol g^{-1} h^{-1} [20]. Su et al. synthesized $BaTiO_3$ nanoparticles with low energy barrier and polarization anisotropy, exhibiting high electromechanical coefficient and hydrogen production rate of 655 μmol g^{-1} h^{-1} [21]. Xu et al. prepared $BaTiO_3$ powders, and only 10 % of escherichia coli survived after 60 min under ultrasonication [23]. Despite numerous inspiring achievements for piezocatalysis, the unsatisfactory catalytic efficiency remains to be a bottleneck for the degradation of organic pollutants.

In general, the free electrons and holes separated inside the piezocatalyst react with dissolved oxygen and water molecules to generate reactive groups that react with dyes in a redox reaction, thereby reducing the water pollution. The catalytic activity of piezocatalysts is determined by the electrical and semiconducting properties of the material, such as polarization enhancement [25], specific surface area [26], heterogeneous structure [27–29], and phase structure [30–32]. It is a well-known fact that piezoelectric ceramics have a high degree of dipole alignment in the region near the phase boundary, leading to easy polarization rotation and significantly improved electrical properties.

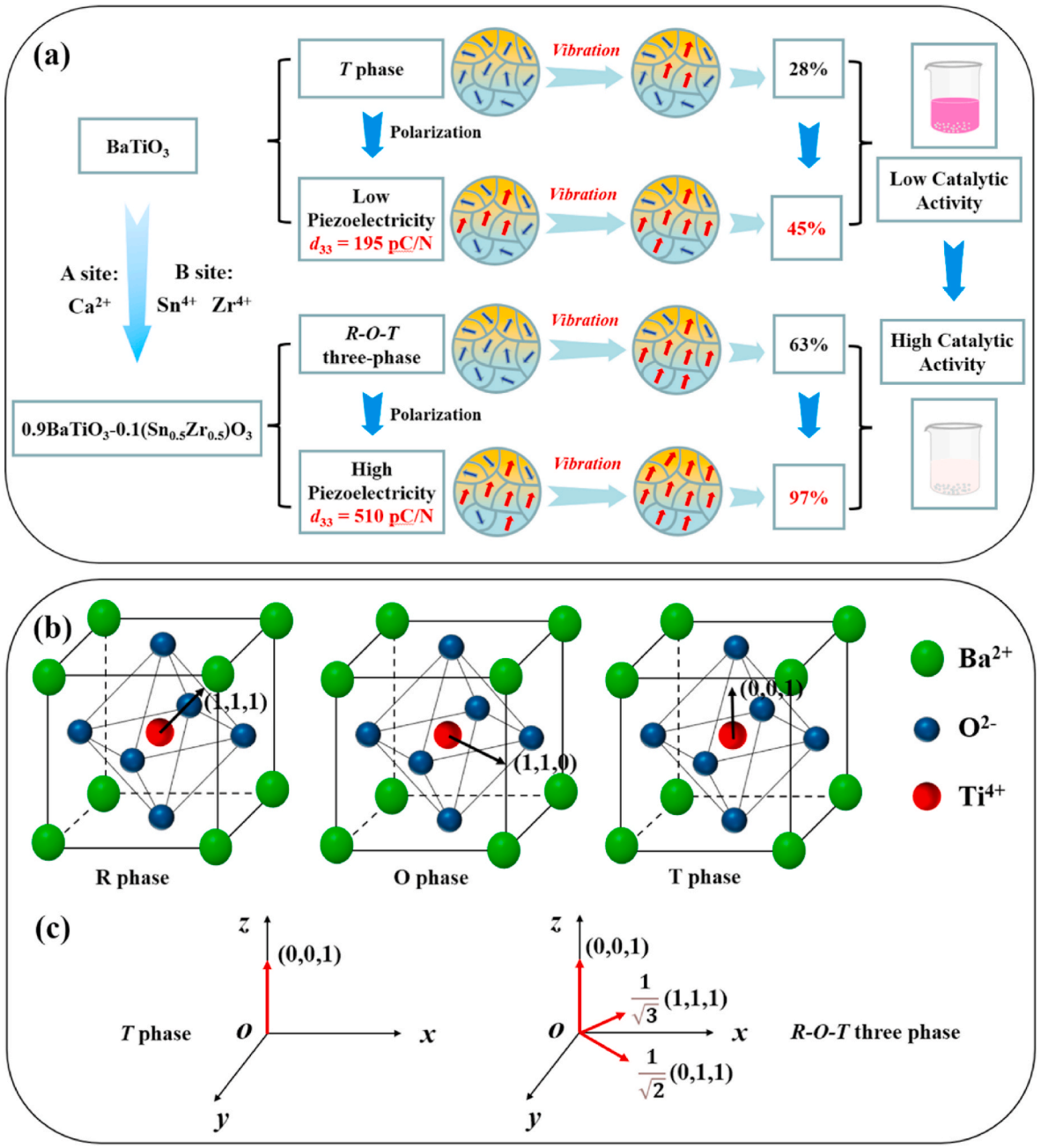

Fig. 1. (a) Design idea of Ca^{2+} and Sn^{4+}, Zr^{4+} co-doped $BaTiO_3$ ceramics for RhB degradation; (b) Spontaneous polarization directions of *R*, *O* and *T* phases; (c) Polarization rotation energy barriers of *T* phase and *R-O-T* three-phase coexistence.

Based on the Landau theory, the macroscopic multiphase coexistence can realize the flattening of Gibbs free energy density distribution. The flattening of the free energy allows the piezocatalyst to separate electrons and holes effectively under ultrasonication, thus improving the piezocatalytic performance. Thus, ceramic systems with multiphase coexistence are expected to exhibit superior piezocatalytic properties. $BaTiO_3$, as a representative piezoelectric material, is an ideal candidate for piezocatalysis because of its superior properties, simple composition, low cost, and easy doping modification. Moreover, extensive studies have shown that ionic substitution of A/B sites of pure $BaTiO_3$ can raise the phase transition temperature of $T_{R\text{-}O}$ and lower $T_{O\text{-}T}$ to construct a phase boundary region with the coexistence of multiphase at room temperature [33–36]. For example, Wang et al. achieved rhombic-orthorhombic-quadratic (*R-O-T*) multiphase coexistence at room temperature by co-doping $BaTiO_3$ with Ca^{2+} and Zr^{4+} to obtain a piezoelectric d_{33} constant of 445 ± 20 pC/N [34]. Yang et al. designed a lead-free ceramic system of (1-*x*)$BaTiO_3$-*x*$CaHfO_3$ and found that the heavy doping led to the coexistence of three ferroelectric phases (*R-O-T*) at $0.08 \geq x \geq 0.06$ [35]. In general, on the one hand, the structure with multiphase coexistence and more twisted crystal declines the symmetry, inducing a dipole moment and a transient polarization reversal under the interference of ultrasonic vibrations. On the other hand, the applied electric field makes the domain flip easier in the ceramics with multiphase coexistence, generating better piezoelectricity. Consequently, regulating the phase structure of piezocatalysts to exhibit the multiphase coexistence is a promising method to achieve outstanding piezocatalytic performance.

In this work, we chose $BaTiO_3$ as the base material and doped Ca^{2+} at the A-site and Zr^{4+}/Sn^{4+} at the B-site in the $BaTiO_3$, respectively, to establish the multiphase coexistence (*R-O-T*) region in (1-*x*)$BaTiO_3$-*x*Ca($Sn_{0.5}Zr_{0.5}$)O_3 (BTCSZ-*x*) ceramics, and systematically investigated the influences of phase boundary and piezoelectric effect on the catalytic degradation performance of dyes. Fig. 1(a) shows that the $BaTiO_3$ ceramic is a tetragonal (*T*) phase structure with a stable crystal structure that is not easily disturbed under ultrasonication. Even though low piezoelectricity is generated after polarization, the catalytic activity is slightly improved but still limited. In the RhB degradation experiment, the degradation rate of pure $BaTiO_3$ increases from 28 % to 45 %. The BTCSZ-0.1 ceramic is a multiphase (*R-O-T*) coexistence structure, in which the crystal structure is distorted. A transient polarization reversal is generated under ultrasonication to obtain the high catalytic activity, while the high piezoelectricity further improves the catalytic activity. The degradation rate of BTCSZ-0.1 ceramic increases from 63 % to 97 % before and after poling. In Figs. 1(b-c), the spontaneous polarization directions of *T*, *O* and *R* phases are <0,0,1>, <1,1,0> and <1,1,1>, respectively. Based on the calculated results of the 6th order Landau-Devonshire model, the polarization vectors of *T*, *O* and *R* phases are <0,0,1>, $\frac{1}{\sqrt{2}}$ <1,1,0> and $\frac{1}{\sqrt{3}}$ <1,1,1>, respectively, showing the coexistence of three ferroelectric phases (*R-O-T*) [35]. The energy barrier of *R-O-T* three-phase coexistence tends to be planarized to ease the polarization rotation. This investigation would provide meritorious insights into the development of piezocatalytic ceramics by compositional and phase boundary modulation to obtain the catalytic performance comparable to nano piezocatalysts.

2. Experimental

2.1. Sample preparation

A series of micron-sized (1-*x*)$BaTiO_3$-*x*Ca($Sn_{0.5}Zr_{0.5}$)O_3 (abbreviated as: BTCSZ-*x*, $x = 0.00, 0.02, 0.04, 0.06, 0.08, 0.10, 0.12$) particles were synthesized by a conventional solid-state method using $BaCO_3$ (99.00 %), ZrO_2 (99.99 %), SnO_2 (99.50 %), $CaCO_3$ (99.99 %) and TiO_2 (99.88 %) as raw materials. Firstly, the ingredients with the calculated weights were ball-milled for 18 h and dried. Secondly, the mixtures were calcined at 1100 °C for 4 h, ball-milled again for 12 h and dried. Then, the materials were mixed with 10 % polyvinyl alcohol (PVA) solution, pressed into disks of 1 mm in thickness and 10 mm in diameter, and burned at 650 °C for 2 h to remove the binder and sintered at 1350 °C for 2 h to form ceramics. Finally, silver paste was brushed on both sides of the ceramic sheet for electrical characterizations.

2.2. Material characterizations

X-ray diffraction (XRD, Miniflex 600, Rigaku, Japan) was used to characterize the crystal structure of BTCSZ-*x* ceramics, and XRD refinement data of BTCSZ-*x* ($x = 0.00, 0.04, 0.10, 0.12$) samples were fitted using GSAS software. The indicated microstructure of BTCSZ-*x* ceramics was observed by a scanning electron microscope (SEM, S4800, Hitachi, Japan). The Raman characteristics of BTCSZ-*x* samples were measured by Raman spectroscopy (LabRam HR Evo-lution, HORIBA Lab ARAMIS, France) with a 532-nm excitation light. The optical absorption spectra were characterized using a UV spectrophotometer (UV, 756 PC, Shanghai, China), and the diffuse reflectance spectra (DRS) of BTCSZ-*x* ($x = 0.0$ and $x = 0.1$) ceramics were tested using a UV diffuse reflectance spectrometer (UV, 2600i, Japan). The X-ray photoelectron spectroscopy (XPS, AXIS Supra, America) was used to record the valence band of BTCSZ-*x* ($x = 0.0$ and $x = 0.1$) ceramics. The temperature (−125 – 100 °C) dependence of dielectric constant (ε_r) was tested at 1 kHz using an LCR instrument (Agilent E4980A, USA). *P-E* loops were tested by a ferroelectric workstation (Premier II, Radiant Technologies Inc, USA) at 10 Hz and room temperature. A quasi-static piezometer (ZJ-6A, Chinese Academic Society, China) was employed to measure the piezoelectric constant, d_{33}.

2.3. Piezocatalytic activity

The effect of phase transition and piezoelectric effect on the catalytic activity of BTCSZ-*x* ceramics was evaluated by degrading dye. BTCSZ-*x* ceramic sheets were poled at a certain level of electric field for 1 h at room temperature in silicone oil bath. The poled ceramic sheets were polished with a sandpaper to remove the silver layer, crushed with a mortar and pestle, and finally sieved using a 300-mesh sieve. First, 100 mg of ceramic particles were scattered into 50 mL of MB, RhB and MO solutions in beakers, respectively. The mixture solution was stirred for 1 h using a magnetic stirrer to bring adsorption-desorption equilibrium between catalyst and dye. Next, the beaker was fixed in an ultrasonic machine (40 kHz, 100 W) for catalytic degradation with the temperature maintained at 25–30 °C 10 mL mixture was collected every 30 min and supernatant was aspirated by centrifugation at 7000 rpm for 5 min. Finally, the absorbance of supernatant was measured by a UV-spectrophotometer. To reveal the active species of dye decomposition, benzoquinone (BQ), disodium ethylenediaminetetraacetate (EDTA-2Na), and isopropyl alcohol (IPA) were adopted as scavengers of superoxide ion ($\bullet O_2^-$), pore (h^+), and hydroxyl radical (•OH), respectively.

3. Results and discussion

3.1. Phase structure

Fig. 2(a) illustrates the XRD spectra of BTCSZ-*x* ($x = 0.00$–0.12) ceramics and gives the standard cards of rhombic (*R*) phase ($BaTiO_3$ PDF#85–0368), orthogonal (*O*) phase ($BaTiO_3$ PDF#81–2198), and tetragonal (*T*) phase ($BaTiO_3$ PDF#81–2201). All ceramics own the ABO_3-type perovskite structure without secondary phase, which indicates that Ca^{2+}, Sn^{4+}, Zr^{4+} have successfully entered the $BaTiO_3$ ceramic lattice and formed a homogeneous solid solution. According to the comparison of XRD spectra and standard cards in Fig. 2(b), the ceramics undergo a phase transition from *T*-phase to *O*-phase and then to *R*-phase as *x* increases. When $x = 0$, the $BaTiO_3$ ceramics mainly display the *T*-phase, which is similar to the literature [37]. As *x* increases from

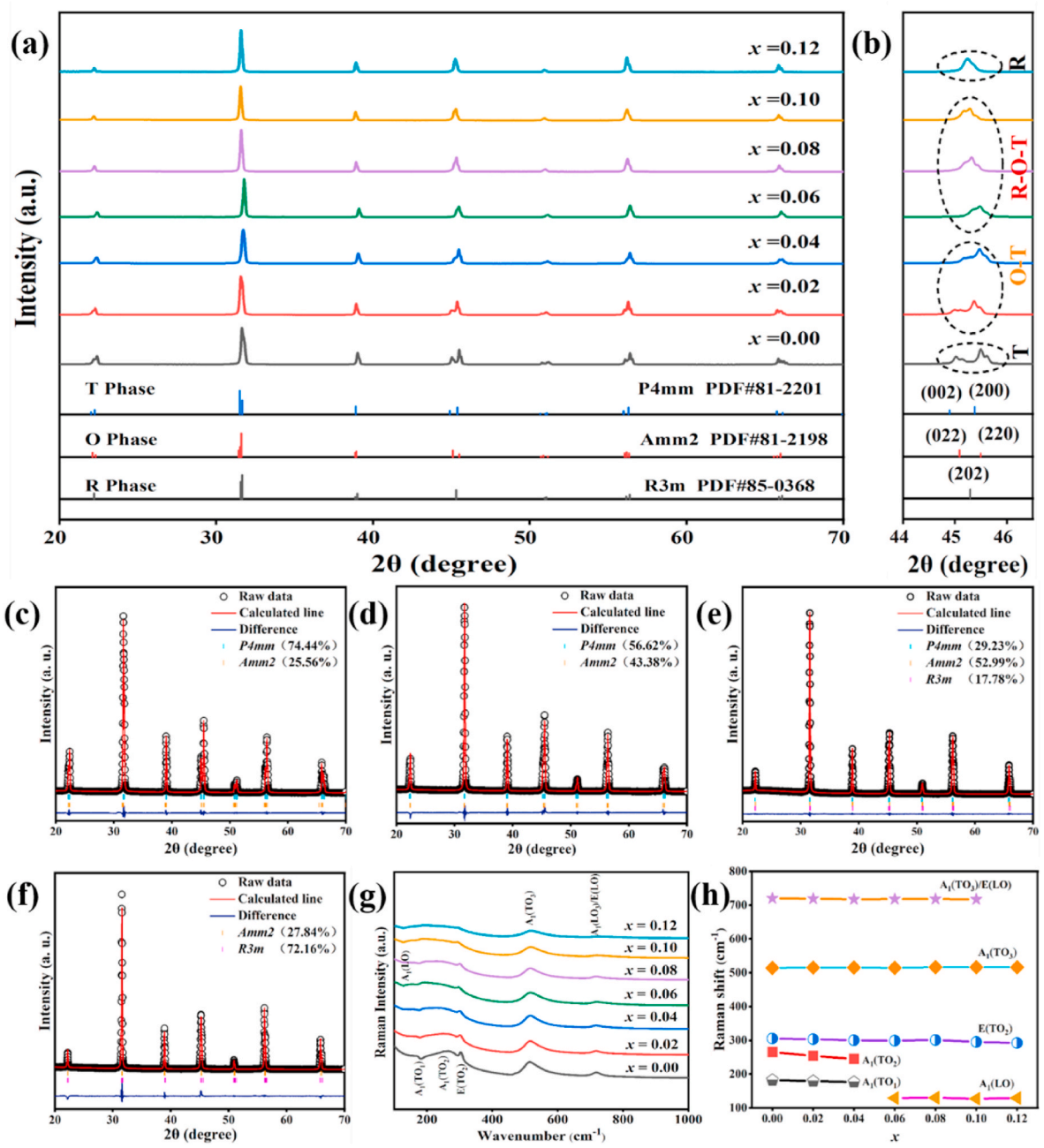

Fig. 2. XRD spectra of BTCSZ-*x* ceramics in the 2θ ranges of (a) 20–70° and (b) 44–46.5°; Refinement results for BTCSZ-*x* ceramics with (c) $x = 0.00$, (d) $x = 0.04$, (e) $x = 0.10$, and (f) $x = 0.12$; (g) Room-temperature Raman spectra of BTCSZ-*x* ceramics; (h) Variation of vibrational modes with *x*.

0.00 to 0.04, the phase structure of ceramics changes from *T*-phase to *O*-phase, and when $0.06 \leq x \leq 0.10$, the ceramics have the coexistence of *R*-*O*-*T* ferroelectric phases. With further increasing *x* to 0.12, the characteristic peaks of *O* and *T* phases disappear. The results illustrate that the doping of $Ca(Sn_{0.5}Zr_{0.5})O_3$ generates a region of ferroelectric multiphase coexistence in $BaTiO_3$ ceramics at room temperature.

In order to characterize the structural phase transition, Rietveld refinement is performed using GSAS software for ceramics with $x = 0.00$, 0.04, 0.10 and 0.12, and the results and corresponding lattice parameters are shown in Figs. 2(c–f) and Table S1. As depicted in Figs. 2 (c–f), the fitted curves are in general agreement with the measured XRD data. For the material with $x = 0$, the final factors of χ^2, R_{wp} and R_p are 2.76, 4.84 % and 3.66 %, respectively, indicating a good match between the tested values and the calculated model. In general, the pure $BaTiO_3$ ceramic usually exhibits a perovskite structure with *T*-phase at room temperature [34,35]. However, phase transitions from *T* to *O* phases exist at lower temperatures. As the ambient temperature in our lab was about 12–15 °C that is close to the phase transition temperature of *T* and *O* phases, the pure $BaTiO_3$ ceramic in this work may have tetragonal and orthorhombic symmetric structures. Fig. 2(c) shows that the *T*-phase dominates with the presence of a small amount of *O*-phase, which is only 25.56 %. A mixture of *O* and *T* phases is refined for BTCSZ-0.04 ceramic, with phase fractions of 56.62 % and 43.38 %, respectively. Notably, BTCSZ-0.10 ceramic possesses the phase contents of *T*-phase, *O*-phase and *R*-phase with 29.23 %, 52.99 % and 17.78 %, respectively, indicating the coexistence of three ferroelectric phases. Besides, when *x* further increases to 0.12, the content of *R*-phase increases and dominates with the disappearance of *T*-phase, while the content of *O*-phase is only 27.84 %. It is reported that the piezoelectric materials are more susceptible to polarization rotation at the multiphase coexistence, which

would enhance the piezoelectric properties [38]. Consequently, it can be concluded that the piezoelectric properties of ceramics may be optimal at BTCSZ-0.1.

To further verify the crystal structure of the ceramics, the room-temperature Raman spectra are measured in the range of 100–1000 cm^{-1} and the vibrational modes against x are tested, as shown in Figs. 2 (g-h). It is known that each pure $BaTiO_3$ cell contains 5 atoms, corresponding to 12 kinds of optical vibrational modes ($3F_{1u} + 1F_{2u}$) [39]. In the pure $BaTiO_3$ ceramic, F_{1u} can split into A_1 and E vibrational modes accompanying with the cleavage of F_{2u} into B_1 and E modes [40]. In Fig. 2(g), the characteristic pattern of the *T*-phase is observed in the ceramics with $x = 0.00$, with characteristic peaks at 182, 265, 305, 514, and 720 cm^{-1}, corresponding sequentially to $A_1(TO_1)$, $A_1(TO_2)$, $E(TO_2)$, $A_1(TO_3)$, $A_1(TO_3)$, and $A_1(LO_3)/E(LO)$. As x increases, the $A_1(TO_1)$ and $A_1(TO_2)$ peaks disappear (Fig. 2(h)), indicating that *T*-phase partially transforms into *O*-phase. When $x \geq 0.06$, the $E(TO_2)$ peak reveals a blue shift and the $A_1(LO)$ vibrational mode appears at near 140 cm^{-1}, demonstrating the presence of *R*-phase. Meanwhile, the characteristic peak $A_1(LO_3)/E(LO_3)$ of *T*-phase persists up to $x = 0.10$, which manifests the coexistence of *R-O-T* at $0.06 \leq x \leq 0.10$. With further increasing x to 0.12, the disappearance of the $A_1(LO_3)/E(LO_3)$ peak and the weakening of other peaks indicate the absence of the *T*-phase and the reduction of the *O*-phase content. In summary, the results and characteristics of Raman and XRD spectra of BTCSZ-*x* ceramics consistently confirm the transformation process from single phase, dual phase to triple phase followed by returning to single phase with the variation of x.

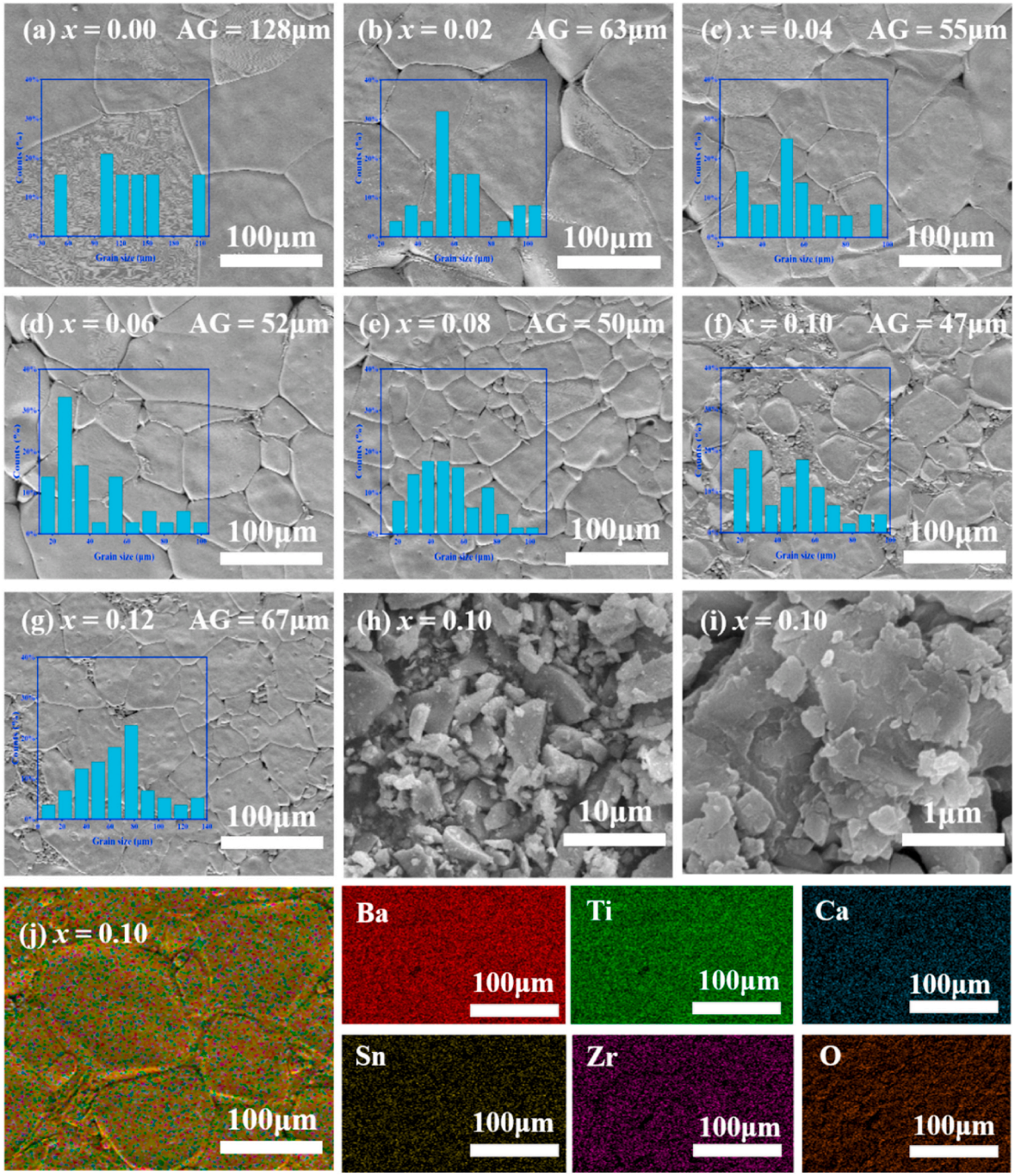

Fig. 3. (a–g) SEM images of surface and average grain sizes of BTCSZ-*x* ceramics at $x = 0.00$–0.12; (h, i) SEM images of BTCSZ-0.1 ceramic particles at different magnifications; (j) EDS elemental mapping of ceramic with $x = 0.10$.

3.2. Morphological analysis

From Figs. 3(a–g), all samples emerge dense and homogeneous microstructures, and the grain size gradually decreases as x increases attributing to the relatively large masses of Sn^{4+} and Zr^{4+} when compared to Ti^{4+}, leading to lower ion mobility [41]. The microstructure of BTCSZ-x ceramics depends on the content of $Ca(Sn_{0.5}Zr_{0.5})O_3$, and the grain size becomes smaller as x increases, indicating that $Ca(Sn_{0.5}Zr_{0.5})O_3$ inhibits the grain growth. It can be seen that the average grain size (AG) decreases dramatically from 128 μm to 47 μm as x increases from 0.00 to 0.10, and then increases slightly from 47 μm to 67 μm as x increases further to 0.12. This is due to the substitution of the small ions of Ti^{4+} by large ions of Sn^{4+} and Zr^{4+}, which increases the lattice strain energy [42] and inhibits the mobility of the grain boundary, thereby inhibiting the grain growth [43]. As exhibited in Figs. 3 (h–i), the BTCSZ-0.1 ceramic particles contain both large and small g rains. The powders have smaller particle clusters and fewer large grains that increase the specific surface area and improve the contact area, resulting in good piezocatalytic activity. Meanwhile, the elemental mapping method is used to observe the elemental distribution of the ceramics. As can be seen from Fig. 3(j) and Table S2, all elements are uniformly distributed with the atomic percentages of Ba, Ti, Ca, Sn, Zr and O of 20.99 %, 23.52 %, 2.02 %, 0.60 %, 0.98 % and 51.88 %, respectively, indicating that Ca^{2+}, Sn^{4+} and Zr^{4+} have successfully diffused into the $BaTiO_3$ ceramic lattice.

3.3. Electrical properties

For further verification of the phase transition behavior induced by the addition of $Ca(Sn_{0.5}Zr_{0.5})O_3$, the temperature dependence of the relative permittivity ε_r is measured and displayed in Figs. 4(a–g). It can be seen that there are two distinct dielectric peaks corresponding to the rhombic-orthogonal ($T_{R\text{-}O}$) phase transition and the orthogonal-quadratic ($T_{O\text{-}T}$) phase transition, respectively. As observed from the inset of Fig. 4(a), the O-T phase transition temperature of pure $BaTiO_3$ is located at 7 °C. Since the actual temperature for XRD measurements is about 12–15 °C, the O-T phase transition has not been completed, resulting in the presence of a small amount of O-phase in the pure $BaTiO_3$ ceramics even at room temperature. As x increases, the phase transition peaks of $T_{R\text{-}O}$ and $T_{O\text{-}T}$ move towards the room temperature. For $x = 0.10$ in Fig. 4(f), the $T_{R\text{-}O}$ and $T_{O\text{-}T}$ peaks merge into a single peak ($T_{R\text{-}O\text{-}T}$). When x further increases to 0.12, the ceramic has only one dielectric peak (T_c). Obviously, certain amounts of Ca^{2+}, Sn^{4+}, Zr^{4+} partially replace the A and B sites of $BaTiO_3$, which disrupts the ferroelectric order and causes non-centrosymmetric cells, inducing the ferroelectric-paraelectric phase transition at room temperature. Similarly, the triple-phase coexistence can be demonstrated by the $T_{R\text{-}O\text{-}T}$ observed at room temperature when $x = 0.10$, which is in accordance with both XRD refinement and Raman results.

Fig. 4(h) illustrates the variations of ε_r and dielectric loss (tanδ) for BTCSZ-x ceramics. As x increases from 0 to 0.12, ε_r increases significantly from 2140 to 24,671. Based on Landau-Ginzburg thermodynamic model calculations [44,45], the polarization anisotropy almost disappears near the ferroelectric-paraelectric phase coexistence region, forming an adaptive state, which is responsible for the high dielectric properties [46–48]. Moreover, tanδ decreases as x increases, reaching a minimum of ~3.74 % at $x = 0.04$, and then tends to remain steady. Considering the asymmetry of crystal structure, the multiphase

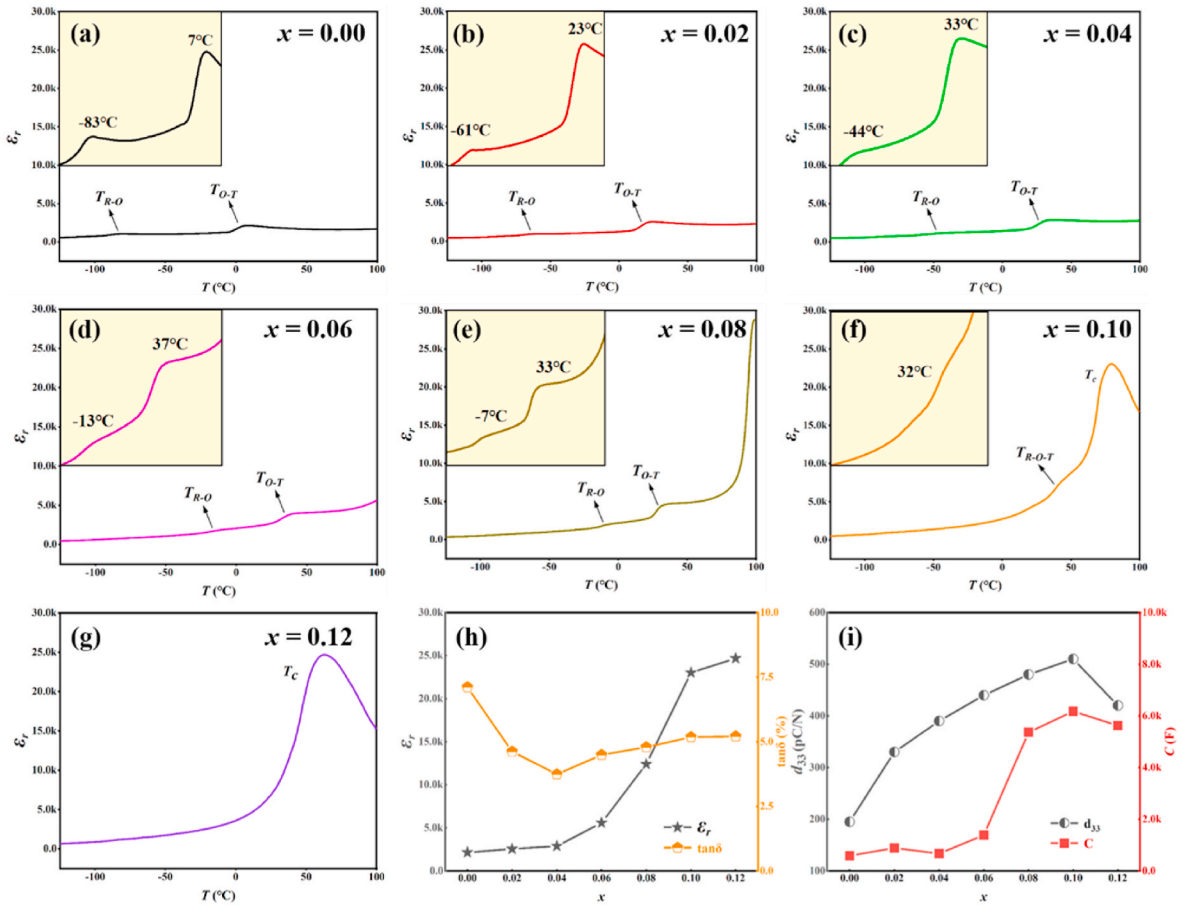

Fig. 4. (a–g) Temperature dependence of relative permittivity ε_r for all samples at 1 kHz, and the insets show the corresponding enlarged phase transition regions in ε_r-T curves; Variations of (h) ε_r and tanδ and (i) d_{33} and C for poled BTCSZ-x ceramics.

coexistence structure deforms the oxygen octahedra and declines the crystal symmetry, inducing a dipole moment to enhance the piezoelectric properties. For Fig. 4(i), the piezoelectric constant (d_{33}) of BTCSZ-0.1 ceramic is 510 pC/N ascribing to the coexistence of the three ferroelectric phases (*R*, *O* and *T* phases). With the advent of *O*-phase and *R*-phase, the piezoelectric properties of ceramics have been improved, which is potentially valuable for applications. Meanwhile, according to the polarization deflection theory proposed by Fu and Cohen [49], the more spontaneous polarization directions would result in the lower polarization rotation energy barrier. As the *R*-phase has eight polarization directions in <111>, the *O*-phase has twelve polarization directions in <110>, and the *T*-phase has six polarization directions in <001>, the coexistence region of three ferroelectric phases (*R*, *O* and *T* phases) possesses 24 polarization directions such that the ferroelectric domains are susceptible to reversal in an external electric field, thus improving the piezoelectric properties [50]. Furthermore, the capacitance (*C*) increases and then decreases as *x* increases, reaching a maximum value of 6173 F at $x = 0.10$.

Figs. 5(a–g) demonstrate the *P-E* hysteresis loops of unpoled BTCSZ-*x* ceramics at 10 Hz. With doping Ca^{2+} at the A-site and Sn^{4+} and Zr^{4+} at the B-site, respectively, the ferroelectric long-range ordering of the ceramics is broken, causing the *P-E* loops increasingly slender. The presence of typical ferroelectric polarization hysteresis loops is a convincing proof for good ferroelectricity in all BTCSZ-*x* ceramics, which originates from the flattening of Lang channel free energy near phase boundary, making the polarization anisotropy lower and the polarization reversal easier [34]. The variations of saturation polarization (P_s), residual polarization (P_r) and coercive field (E_c) with *x* are represented in Fig. 5(h). It is a well-known fact that the crystal structure of perovskite materials affects the ferroelectric/piezoelectric properties profoundly [4]. According to the XRD refinement results, the ion substitutions [Ca^{2+} (1.34 Å) for Ba^{2+} (1.61 Å) at the A site and Sn^{4+} (0.69 Å)/Zr^{4+} (0.72 Å) for Ti^{4+} (0.605 Å) at the B site] with different ionic radii distort the crystal structure of BTCSZ-*x* ceramics. For example, the more contorted oxygen octahedron in BTCSZ-0.1 ceramic induces more dipole moment when compared to BTCSZ-0 ceramic, contributing to the polarization intensity in both rhombic and orthorhombic phases. Thus, P_s and P_r increase with *x*, reaching maximum values of 34.2 μC/cm^2 and 15.8 μC/cm^2, respectively, at $x = 0.08$. In addition, E_c increases and then descends with *x*, first reaching a maximum of 2.8 kV/cm at $x = 0.02$ followed by a gradual decrease to 1.0 kV/cm.

3.4. Piezocatalytic properties

The piezocatalytic performance of BTCSZ-*x* ceramic particles are evaluated using their degradation capability of organic dyes as an index. RhB is used as the target pollutant. Both unpoled (UP) and poled (P) BTCSZ-*x* ceramic particles are tested for the degradation of RhB (5 mg/L), and the UV absorption spectra of the dye solution at different degradation durations are shown in Fig. S1. The RhB absorption intensity exhibits a gradual decline using all ceramic samples with increasing ultrasonic time, indicating the piezocatalytic degradation of RhB of BTCSZ-*x* ceramics. The variation of absorption peaks at ~554 nm is correlated to the time-dependent degradation activity of RhB for all samples, as displayed in Fig. 6. From Fig. 6(a) and (d), both unpoled and poled pure $BaTiO_3$ ceramic ($x = 0.00$) exhibit a limited decomposition capability for RhB. The catalytic activity is significantly enhanced for the ceramic particles with increasing *x*. This indicates that the increasing doping content aggrandizes the confusion of $BaTiO_3$-based piezoelectric materials, and the change of phase boundary itself induced from the phase transition enhances the catalytic activity. When compared to unpoled ceramic particles (Fig. 6(a)), the catalytic activity of poled particles (Fig. 6(d)) is significantly enhanced, which indicates that the polarization process endows the piezoelectric ceramics with certain piezoelectric properties, resulting in the enhancement of decomposition effect of RhB. Especially, the poled BTCSZ-0.1 ceramic particles could almost decompose all RhB within 120 min, demonstrating the optimal catalytic activity.

Generally, the piezocatalytic activity follows the Langmuir-Hinshelwood model, as shown in Equation (1).

$$C = C_0 \times e^{-kt} \tag{1}$$

where *t* is the ultrasonic time, C_0 and *C* are initial concentration and residual concentration after reaction with the dye solution for *t* minutes, respectively, and *k* presents the reaction rate constant [4]. The reaction rate constant is usually adopted to analyze the first-order kinetic function of the catalytic reaction, i.e., Equation (2) [15]:

$$-\ln\left(C / C_o\right) = kt \tag{2}$$

A linear fitting of $-\ln(C/C_0)$ to *t* is performed to obtain the first-order kinetic function. It is concluded that the kinetic analysis results agree well with the first-order kinetic function data in the comparison of linear fittings between unpoled (Fig. 6(b)) and poled (Fig. 6(e)) samples. The fitting results demonstrate that the reaction rate constants of unpoled

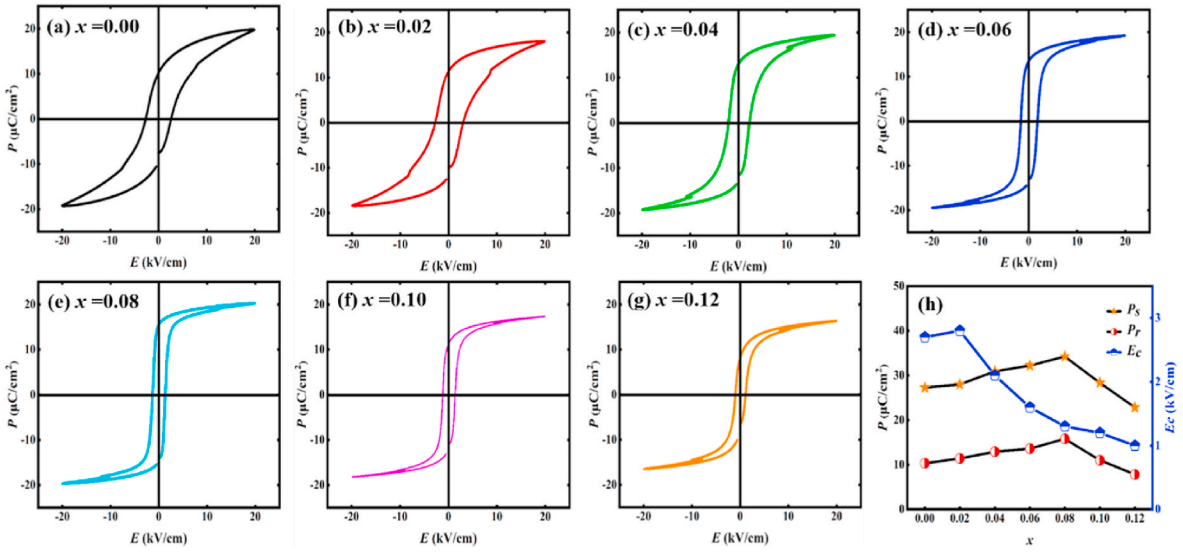

Fig. 5. (a–g) *P-E* hysteresis loops and (h) variations of P_s, P_r and E_c for unpoled BTCSZ-*x* ceramics.

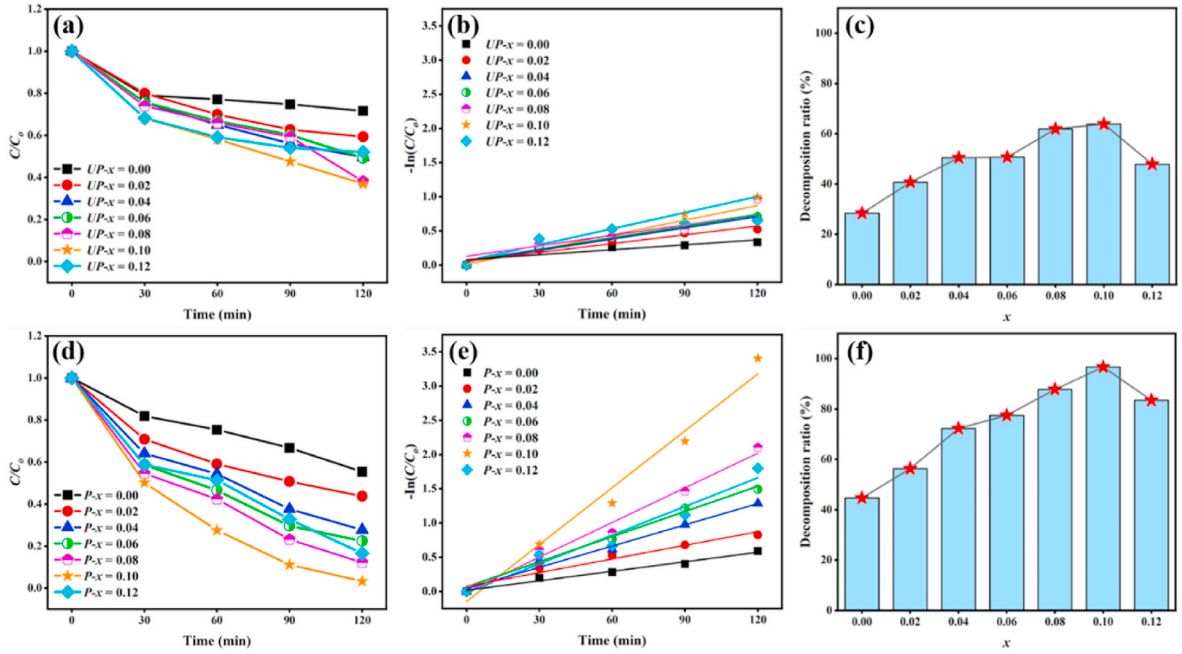

Fig. 6. Piezocatalytic activity of (a–c) unpoled and (d–f) poled BTCSZ-*x* ceramic particles against 5 mg/L RhB: (a, d) C/C_0 and (b, e) -ln(C/C_0) versus time and (c, f) degradation rate in 120 min for samples with different fractions.

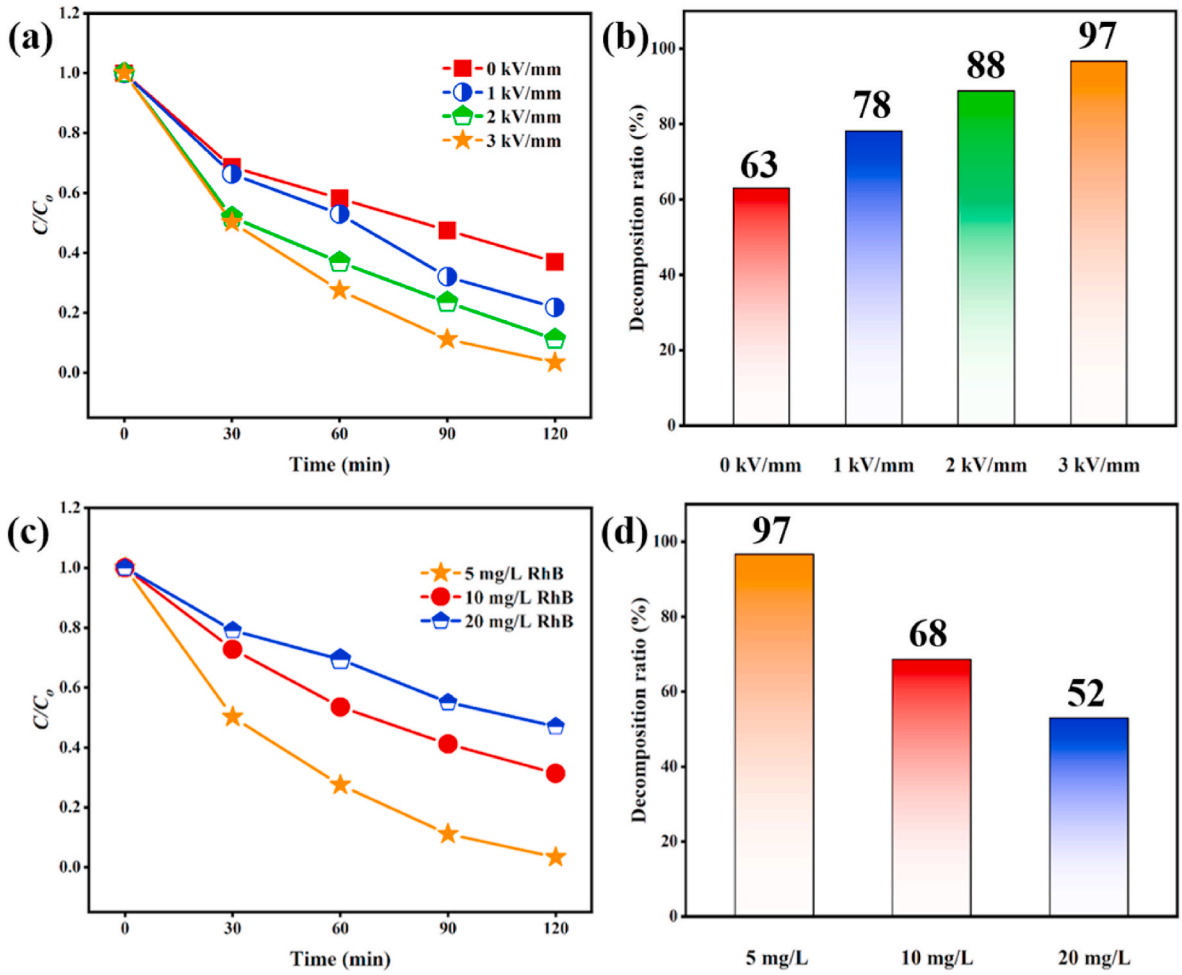

Fig. 7. (a) Piezocatalytic activity of BTCSZ-0.1 ceramic particles against 5 mg/L RhB at different electric fields and (b) the corresponding decomposition ratios in 120 min; (c) Piezocatalytic activity of BTCSZ-0.1–3 kV/mm ceramic particles against RhB concentration and (d) the corresponding decomposition ratios in 120 min.

and poled BTCSZ 0.1 ceramics for 5 mg/L RhB are 8.3×10^{-3} min^{-1} and 28.4×10^{-3} min^{-1}, respectively. Fig. 6(c, f) show the decomposition rates of unpoled and poled BTCSZ-*x* ceramic particles for 5 mg/L RhB, and the decomposition rate (*D*) of the dye is calculated as follows [15]:

$$D = (A_0 - A_t) / A_t \times 100\% \quad (3)$$

where A_0 and A_t are the maximum absorbance at ~554 nm at 0 min and *t* min, respectively. The decomposition ratios of unpoled and poled BTCSZ-*x* ceramics particles against 5 mg/L RhB after degradation for 120 min are shown in Table S3. In summary, with the increasing content of $Ca(Sn_{0.5}Zr_{0.5})O_3$, the $BaTiO_3$-based piezoelectric material transforms from single-phase to multiphase such that the crystal structure becomes distorted with reduced symmetry and increases the degree of internal disorder. The ceramic particles are then highly susceptible to external disturbances. Under the action of ultrasound, the unpoled ceramic particles are deformed to induce the piezoelectric effect. Consequently, non-zero net polarization would occur, resulting in degradation of the dye. When the ceramics are subjected to an applied electric field, the intrinsic piezoelectric properties of poled ceramics accelerate the electron mobility and slow down the electron-hole complexation simultaneously, thus further enhancing the catalytic activity. On the contrary, when *x* increases to 0.12, the piezoelectric properties of BTCSZ-0.12 ceramic degrade, leading to the decline of catalytic performance as the BTCSZ-0.12 ceramic is not in the multiphase coexistence region. Thus, the BTCSZ-0.1 ceramic with the optimal doping composition is used as the catalyst for the subsequent experiments.

To investigate the effect of electric field on the catalytic activity of piezoelectric materials, the degradation of RhB using BTCSZ-0.1 material poled at various electric fields is verified. The BTCSZ-0.1 ceramics poled at 0 kV/mm, 1 kV/mm, 2 kV/mm, and 3 kV/mm are named as BTCSZ-0.1-0 kV/mm, BTCSZ-0.1–1 kV/mm, BTCSZ-0.1–2 kV/mm, and BTCSZ-0.1–3 kV/mm, respectively. All experiments are kept at atmospheric pressure and ~25 °C. The analysis of the results in Fig. 7(a) concludes that the piezocatalytic activity of BTCSZ-0.1 material gradually increases with the electric field. The best degradation of RhB at 5 mg/L is achieved after poled at an external electric field of 3 kV/mm. The UV absorption spectra of RhB (5 mg/L) degraded using BTCSZ-0.1 ceramic poled at different electric fields are presented in Fig. S2 and the corresponding decomposition ratios are delineated in Fig. 7(b). Fig. 7(b) illustrates the decomposition ratios of 5 mg/L RhB using BTCSZ-0.1-0 kV/mm, BTCSZ-0.1–1 kV/mm, BTCSZ-0.1–2 kV/mm, and BTCSZ-0.1–3 kV/mm are 63.04 %, 78.22 %, 88.85 %, and 96.67 %, respectively. The results display that the degradation capacity of BTCSZ-0.1 ceramic particles increase with the electric field. This is owing to the enhancement of piezoelectric properties of BTCSZ-0.1 ceramics poled at higher electric fields, leading to better catalytic performance. The effect of the dye concentration on the piezocatalytic activity is evaluated by comparing the degradation of RhB with different initial concentrations (C_0 = 10 and 20 mg/L) as shown in Figs. S2(e–f). From Fig. 7(c), the degradation capability of BTCSZ-0.1–3 kV/mm decreases along with the increasing C_0. This may be ascribed to the finite quantities of catalytic active sites for a certain number of ceramic particles. The increasing initial dye concentration may exceed the capacity of active sites, leading to the drop of catalytic efficiency. Furthermore, when there is a large number of RhB molecules in the reaction system, the charged RhB molecules can occupy the active sites through electrostatic interactions, thus weakening the built-in electric field of the ceramic particles and leading to the reduction of active radicals. Besides, we investigated the effect of particle size on the catalytic performance. Fig. S6 shows that the degradation ability of BTCSZ-0.1 ceramic increases when the particles become smaller. This is due to the fact that smaller ceramic particles have a larger contact area with the solution, thus degrading the dye faster.

To further verify the catalytic performance of BTCSZ-0.1–3 kV/mm, two other typical organic dyes, methylene blue (MB) and methyl orange (MO), are utilized as the target pollutants for degradation. The temporal variations of the absorption spectra of the three dye solutions are shown in Figs. S3(a–b). The absorption spectra of the three dye solutions with the same concentration and the corresponding degradation rates using BTCSZ-0.1–3 kV/mm are demonstrated in Figs. 8(a-b). It can be observed that the degradation rates of MB (93 %) and MO (73 %) are both lower than that of RhB (97 %) in 120 min, indicating that BTCSZ-*x* exhibits better catalytic performance for cationic dyes (RhB, MB). Considering the similar specific surface area, the variation in catalytic activity is attributed to their apparently different molecular structures that are shown in Fig. S4. Owing to electrostatic interactions, the cationic dye molecules tend to attach to the negatively polarized surface where the negative charge is located [51]. During piezoelectric catalysis, electrons and holes are separated and transferred to the positively and negatively polarized surfaces, respectively, while the positive valence band in the BTCSZ-0.1 material promotes the transfer of holes from the negatively polarized surface to the reactive groups, inducing much excellent catalytic performance for cationic dyes. The importance of polarity matching in piezocatalysis is revealed, which has been studied accordingly in other piezoelectric materials [8]. As the stability of piezocatalyst becomes critical in practical applications, the cyclability of BTCSZ-0.1–3 kV/mm is also evaluated. The piezocatalytic activity and corresponding degradation rates in four degradation cycles of 5 mg/L RhB are shown in Fig. S3 (c–f) and Figs. 8(c-d), respectively. To avoid the adsorption of dye in the catalytic activity, the ceramic particles are washed with deionized water and dried before the next cycle. The decomposition ratio remains 84 % after four cycles of treatment, indicating that the piezocatalyst in this study has good cycling stability and can be applied as a promising selection for environmental remediation.

3.5. Catalysis mechanism

To elucidate the role of reactive substances in piezocatalysis, a series of controlled experiments are carried out by introducing different radical scavengers into the BTCSZ-0.1 reaction system. As seen in Figs. 9 (a-b), benzoquinone (BQ) and isopropyl alcohol (IPA) additives burst the $\bullet O_2^-$ and •OH radicals, respectively, thus significantly inhibiting the piezocatalytic degradation activity. Meanwhile, ethylenediaminedisodium tetraacetate (EDTA-2Na) as a scavenger of h^+ has a certain inhibitory effect on the degradation of RhB. The results signify that all $\bullet O_2^-$, •OH and h^+ radicals have implications for the dye degradation reaction, wherein $\bullet O_2^-$ and •OH are the dominant active substances. It is widely known that the catalytic capability of semiconductors is dependent on both the valence band potential and conduction band potential. The electronic structure of BTCSZ-*x* ($x = 0.0$ and $x = 0.1$) samples are evaluated using UV–vis diffuse reflectance spectroscopy. From Fig. 9(c) and Fig. S5(a), the band gaps of BTCSZ-*x* ($x = 0.0$ and $x = 0.1$) samples are obtained from the auc's equation [15,52]:

$$(\alpha h\nu)^2 = A(h\nu - E_g) \quad (4)$$

where α, h, ν, E_g, and A are the absorption coefficient, Planck's constant, photon frequency, bandgap, and absorption constant, respectively. An index of 2 represents a direct bandgap semiconductor, which belongs to the ABO_3 crystal structure. From the insets of Fig. 9(c) and Fig. S5(a), the band gap (E_g) of BTCSZ-0.0 and BTCSZ-0.1 ceramic are 2.98 eV and 3.12 eV, respectively. To further determine the energy band diagram, the valence bands of BTCSZ-0.0 and BTCSZ-0.1 samples are examined using XPS. The top of the valence band position (E_{VB}) of the BTCSZ-0.1 sample is calculated to be +2.25 eV, which is more positive than OH^-/•OH (+1.9 eV vs. RHE). According to the empirical formula,

$$E_g = E_{VB} - E_{CB} \quad (5)$$

the bottom of the conduction band E_{CB} is −0.87 eV, which is more negative than $\bullet O_2^-/O_2$ (−0.33 eV vs. RHE). Similarly, the top of the valence band position (E_{VB}) of the BTCSZ-0.0 sample is calculated to be

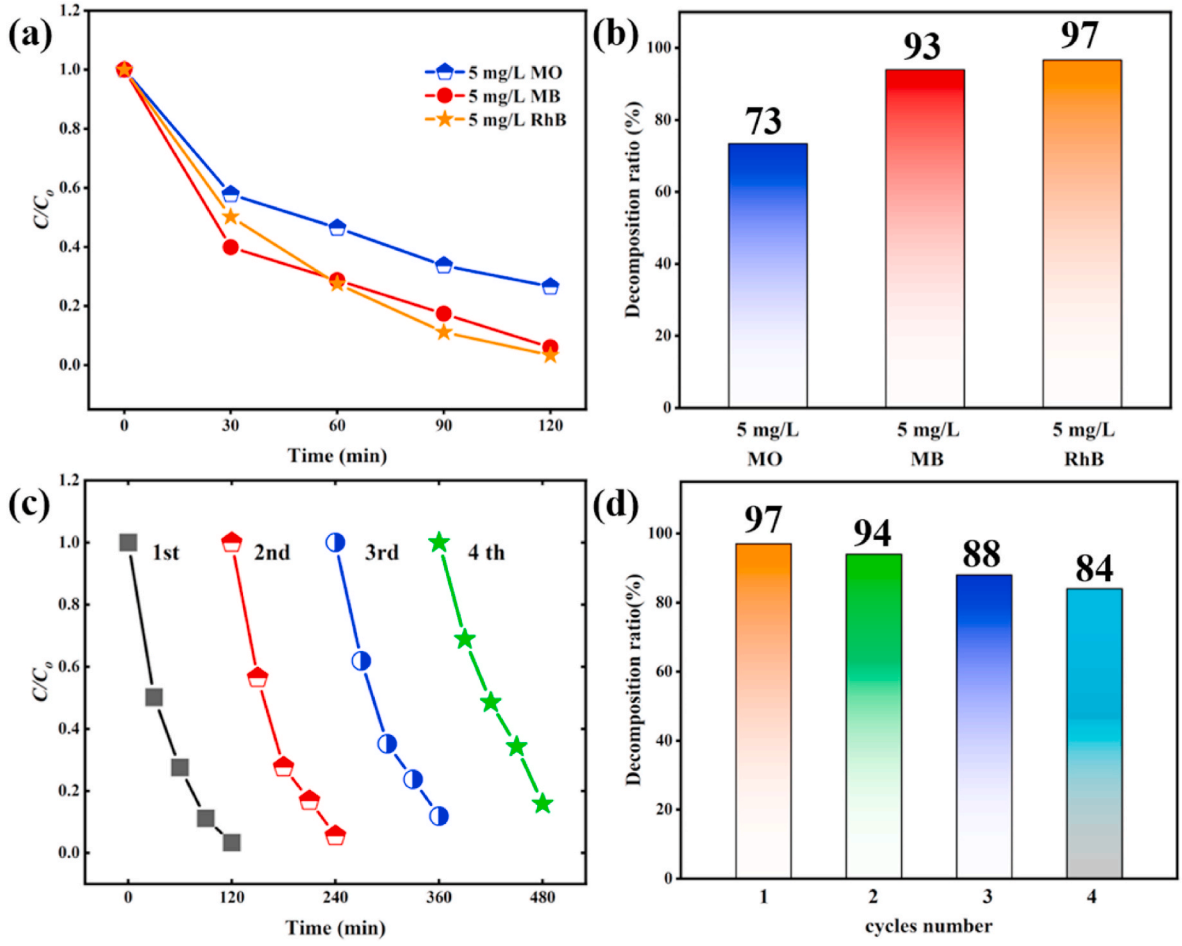

Fig. 8. (a) Piezocatalytic activity of BTCSZ-0.1–3 kV/mm for different types of dyes and (b) its decomposition ratio in 120 min; (c) Recyclability of BTCSZ-0.1–3 kV/mm for the degradation of 5 mg/L RhB and (d) its decomposition ratio after four cycles.

+1.82 eV, and the bottom of the conduction band E_{CB} is −1.16 eV. Accordingly, a schematic diagram of the band gap energy level of the BTCSZ-0.0 and BTCSZ-0.1 samples are portrayed in Figs. S5(c and d). For the BTCSZ-0.0 sample, the E_{VB} (+1.82 eV) is lower than the redox potential of OH^-/•OH (+1.9 eV vs. RHE), which is insufficient for oxidation reaction. Hence, the catalytic activity of BTCSZ-0.1 sample is greatly enhanced when compared to that of BTCSZ-0.0 sample. Based on the above discussion, the mechanism of piezocatalytic degradation of RhB is speculated as illustrated in Fig. 9(e): when the BTCSZ-*x* ceramic particles are subjected to external stresses provided by ultrasonic vibration, the piezoelectric effect generates the built-in electric field to induce the separation and migration of electron-hole pairs [15,16,52]. The electrons on the CB would react with O_2 to form $\bullet O_2^-$ radicals while the holes on the VB react OH^- in water to form •OH radicals, suggesting that the large piezoelectric potential difference in the BTCSZ crystal would likely to induce the migration of electrons and holes to the crystal surface. Easier and faster formation of $\bullet O_2^-$ and •OH radicals can be executed on the surface of poled micron-sized BTCSZ-0.1 particles. Under the impact of external ultrasonic vibration, $\bullet O_2^-$ and •OH radicals are highly oxidized, in which the electrons and holes can excite a series of redox reactions to degrade the RhB molecules. In conclusion, a series of reaction mechanisms in the piezocatalysis process can be described as follows:

$$BTCSZ \xrightarrow{\text{Vibration}} BTCSZ + e^- + h^+ \quad (6)$$

$$O_2 + e^- \rightarrow \bullet O_2^- \quad (7)$$

$$OH^- + h^+ \rightarrow \bullet OH \quad (8)$$

$$\bullet O_2^- + \bullet OH + RhB \rightarrow Degradation \quad (9)$$

In conclusion, the change of phase boundaries in piezoelectric ceramics plays a key role in dye degradation, which can greatly enhance the piezoelectric catalytic activity.

4. Conclusion

In summary, novel BTCSZ-*x* piezoelectric ceramics have been constructed through phase boundary strategies to improve the piezocatalytic activity. The doping of $Ca(Sn_{0.5}Zr_{0.5})O_3$ into $BaTiO_3$ induces the phase transition from single phase to multiphase (coexistence of *R*-*O*-*T* ferroelectric phases), distorting the crystal structure to produce a dipole moment and descend the polarization rotation energy to generate outstanding piezoelectric and piezocatalytic performance. Consequently, the BTCSZ-0.1 ceramic exhibits degradation rates of 97 % for RhB, 93 % for MB and 73 % for MO, respectively. Especially, the RhB is degraded by 97 % within 120 min under ultrasonication, suggesting the excellent piezocatalytic performance of BTCSZ-0.1 ceramic for organic pollutants. In this paper, we propose the application of BT-based piezoelectric materials for environmental remediation and provide a strategy for synthesizing advanced catalysts for future industrial applications.

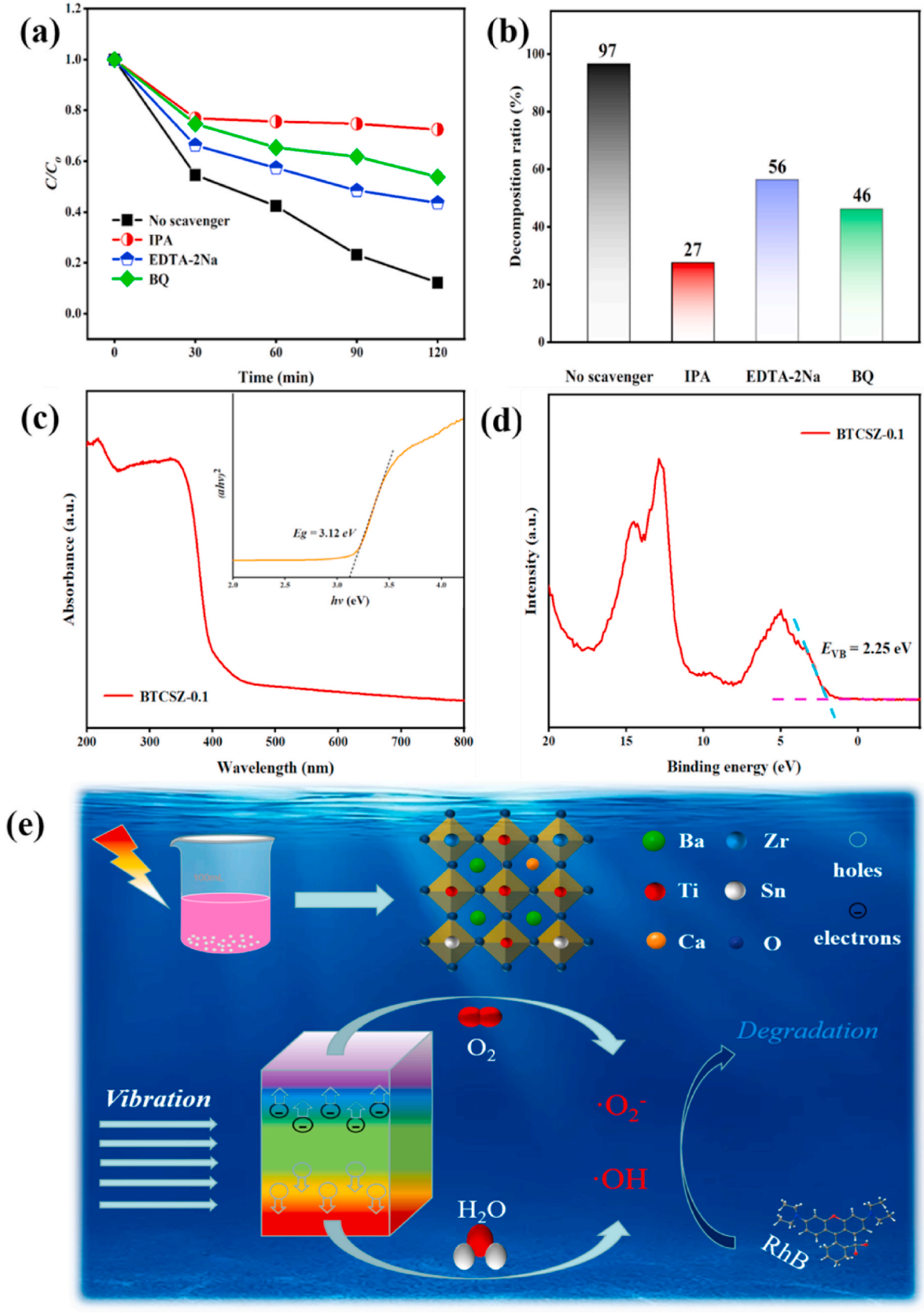

Fig. 9. (a) Effect of free radical scavengers on the piezocatalytic performance of BTCSZ-0.1–3 kV/mm on the degradation of RhB and (b) the corresponding decomposition ratios in 120 min; UV–Vis diffuse reflectance absorption spectrum of BTCSZ-0.1 sample including (c) $(\alpha h\upsilon)^2$ as a function of photon energy ($h\upsilon$), and (d) XPS valence band spectra for BTCSZ-0.1 sample; (e) Schematic diagram of piezocatalytic degradation of RhB using BTCSZ-*x* ceramic.

Declaration of competing interest

The authors declare that they have no known competing financial interests or personal relationships that could have appeared to influence the work reported in this paper.

Acknowledgements

This work was supported by Natural Science Foundation of Sichuan Province (2022NSFSC0222) and Sichuan Science and Technology Program (2023NSFSC0439).

Appendix A. Supplementary data

Supplementary data to this article can be found online at https://doi.org/10.1016/j.ceramint.2023.11.013.

References

[1] Q. Liu, Q. Hu, D. Zhai, Q. Sun, H. Luo, D. Zhang, Superior photo-piezoelectric catalytic performance using $Bi_{0.5}Na_{0.5}TiO_3$@ $BiVO_4$ based cloth, J. Mater. Chem. A 9 (2021) 17841–17854.
[2] M. Sharma, R. Vaish, Piezo/pyro/photo-catalysis activities in $Ba_{0.85}Ca_{0.15}(Ti_{0.9}Zr_{0.1})_{1-x}Fe_xO_3$ ceramics, J. Am. Ceram. Soc. 104 (2021) 45–56.
[3] R. Huang, J. Wu, E. Lin, Z. Kang, N. Qin, D. Bao, A new strategy for large-scale synthesis of $Na_{0.5}Bi_{0.5}TiO_3$ nanowires and their application in piezocatalytic degradation, Nanoscale Adv. 3 (2021) 3159–3166.
[4] A. Zhang, Z. Liu, B. Xie, J. Lu, K. Guo, S. Ke, L. Shu, H. Fan, Vibration catalysis of eco-friendly $Na_{0.5}K_{0.5}NbO_3$-based piezoelectric: an efficient phase boundary catalyst, Appl. Catal. B Environ. 279 (2020), 119353.
[5] M. Ahmad, X. Quan, S. Chen, H. Yu, Z. Zeng, Operating redox couple transport mechanism for enhancing photocatalytic H_2 generation of Pt and CrO_x-decorated ZnCdS nanocrystals, Appl. Catal. B Environ. 283 (2021), 119601.
[6] B. Zhai, Y. Chen, Y. Liang, Y. Gao, J. Shi, H. Zhang, Y. Li, Modifying Ag_3VO_4 with metal-organic frameworks for enhanced photocatalytic activity under visible light, Mater. Chem. Phys. 239 (2020), 122078.
[7] Z. Liang, C.-F. Yan, S. Rtimi, J. Bandara, Piezoelectric materials for catalytic/photocatalytic removal of pollutants: recent advances and outlook, Appl. Catal. B Environ. 241 (2019) 256–269.
[8] X. Zhou, Q. Sun, D. Zhai, G. Xue, H. Luo, D. Zhang, Excellent catalytic performance of molten-salt-synthesized $Bi_{0.5}Na_{0.5}TiO_3$ nanorods by the piezo-phototronic coupling effect, Nano Energy 84 (2021), 105936.
[9] K. Chen, Q. Fan, C. Chen, Z. Chen, A. Alsaedi, T. Hayat, Insights into the crystal size and morphology of photocatalysts, J. Colloid Interface Sci. 538 (2019) 638–647.
[10] H. Li, Y. Zhou, W. Tu, J. Ye, Z. Zou, State-of-the-art progress in diverse heterostructured photocatalysts toward promoting photocatalytic performance, Adv. Funct. Mater. 25 (2015) 998–1013.
[11] Z. Wei, M. Janczarek, M. Endo, K. Wang, A. Balčytis, A. Nitta, M.G. Méndez-Medrano, C. Colbeau-Justin, S. Juodkazis, B. Ohtani, Noble metal-modified faceted anatase titania photocatalysts: octahedron versus decahedron, Appl. Catal. B Environ. 237 (2018) 574–587.
[12] S. Tu, Y. Guo, Y. Zhang, C. Hu, T. Zhang, T. Ma, H. Huang, Piezocatalysis and piezo-photocatalysis: catalysts classification and modification strategy, reaction mechanism, and practical application, Adv. Funct. Mater. 30 (2020), 2005158.
[13] C. Chen, Y. Wang, Z.-Y. Li, C. Liu, W. Gong, Q. Tan, B. Han, F.-Z. Yao, K. Wang, Evolution of electromechanical properties in Fe-doped $(Pb,Sr)(Zr,Ti)O_3$ piezoceramics, Journal of Advanced Ceramics 10 (2021) 587–595.
[14] Z. Cen, S. Bian, Z. Xu, K. Wang, L. Guo, L. Li, X. Wang, Simultaneously improving piezoelectric properties and temperature stability of $Na_{0.5}K_{0.5}NbO_3$(KNN)-based ceramics sintered in reducing atmosphere, Journal of Advanced Ceramics 10 (2021) 820–831.
[15] M. Zhu, S. Li, H. Zhang, J. Gao, K. Kwok, Y. Jia, L.-B. Kong, W. Zhou, B. Peng, Diffused phase transition boosted dye degradation with $Ba(Zr_xTi_{1-x})O_3$ solid solutions through piezoelectric effect, Nano Energy 89 (2021), 106474.
[16] X. Liang, X. Shi, X. Zou, Z. Wang, Z. Cheng, Synergetic degradation of organic dyes and Cr(VI) by the piezocatalytic BZT-xBCT, New J. Chem. 46 (2022) 9184–9194.
[17] K. Wang, B. Li, C. Zhao, S. Yuan, C. Zhang, X. Liang, J. Wang, Y. Wu, Y. He, A novel NiO/$BaTiO_3$ heterojunction for piezocatalytic water purification under ultrasonic vibration, Ultrason. Sonochem. 92 (2023), 106285.
[18] R. Zhang, X. Wu, Y. Li, W. Shao, Y. Zhang, Z. Liu, J. Nie, J. Tan, W. Ye, Enhanced piezo-photocatalytic performance by piezoelectric and visible light photoexcitation coupling through piezoelectric $Na_{0.5}Bi_{0.5}TiO_3$ micron crystals, RSC Adv. 10 (2020) 7443–7451.
[19] P.T.T. Phuong, D.-V.N. Vo, N.P.H. Duy, H. Pearce, Z.M. Tsikriteas, E. Roake, C. Bowen, H. Khanbareh, Piezoelectric catalysis for efficient reduction of CO_2 using lead-free ferroelectric particulates, Nano Energy 95 (2022), 107032.
[20] Y. Zhang, P.T.T. Phuong, N.P.H. Duy, E. Roake, H. Khanbareh, M. Hopkins, X. Zhou, D. Zhang, K. Zhou, C. Bowen, Polarisation tuneable piezo-catalytic activity of Nb-doped PZT with low Curie temperature for efficient CO_2 reduction and H_2 generation, Nanoscale Adv. 3 (2021) 1362–1374.
[21] R. Su, H.A. Hsain, M. Wu, D. Zhang, X. Hu, Z. Wang, X. Wang, F.t. Li, X. Chen, L. Zhu, Nano-ferroelectric for high efficiency overall water splitting under ultrasonic vibration, Angew. Chem. Int. Ed. 58 (2019) 15076–15081.
[22] Y. Jiang, C.Y. Toe, S.S. Mofarah, C. Cazorla, S.L. Chang, Y. Yin, Q. Zhang, S. Lim, Y. Yao, R. Tian, Efficient cocatalyst-free piezo-photocatalytic hydrogen evolution of defective $BaTiO_{3-x}$ nanoparticles from seawater, ACS Sustain. Chem. Eng. 11 (2023) 3370–3389.
[23] J. Xu, T. Zang, D. Du, S. Kumar, M. Sharma, R. Vaish, Effect of poling on piezocatalytic removal of muti-pollutants using $BaTiO_3$, J. Am. Ceram. Soc. 104 (2021) 1661–1668.
[24] S. Chen, P. Zhu, L. Mao, W. Wu, H. Lin, D. Xu, X. Lu, J. Shi, Piezocatalytic medicine: an emerging frontier using piezoelectric materials for biomedical applications, Adv. Mater. (2023), 2208256.
[25] J. Ma, Y. Jia, L. Chen, Y. Zheng, Z. Wu, W. Luo, M. Jiang, X. Cui, Y. Li, Dye wastewater treatment driven by cyclically heating/cooling the poled $(K_{0.5}Na_{0.5})NbO_3$ pyroelectric crystal catalyst, J. Clean. Prod. 276 (2020), 124218.
[26] Y. Huan, X. Wang, W. Hao, L. Li, Enhanced photocatalysis activity of ferroelectric $KNbO_3$ nanofibers compared with antiferroelectric $NaNbO_3$ nanofibers synthesized by electrospinning, RSC Adv. 5 (2015) 72410–72415.
[27] H. Meng, Z. Chen, Z. Lu, X. Wang, Piezoelectric effect enhanced plasmonic photocatalysis in the Pt/$BaTiO_3$ heterojunctions, J. Mol. Liq. 369 (2023), 120846.
[28] X. Xu, X. Lin, F. Yang, S. Huang, X. Cheng, Piezo-photocatalytic activity of $Bi_{0.5}Na_{0.5}TiO_3$@TiO_2 composite catalyst with heterojunction for degradation of organic dye molecule, J. Phys. Chem. C 124 (2020) 24126–24134.
[29] H. Zheng, X. Li, K. Zhu, P. Liang, M. Wu, Y. Rao, R. Jian, F. Shi, J. Wang, K. Yan, Semiconducting $BaTiO_3$@C core-shell structure for improving piezo-photocatalytic performance, Nano Energy 93 (2022), 106831.
[30] J. Li, X. Wei, X.-x. Sun, R. Li, C. Wu, J. Liao, T. Zheng, J. Wu, A novel strategy for excellent piezocatalytic activity in lead-free $BaTiO_3$-based materials via manipulating the multiphase coexistence, ACS Appl. Mater. Interfaces 14 (2022) 46765–46774.
[31] X.-x. Sun, R. Li, Z. Yang, N. Zhang, C. Wu, J. Li, Y. Chen, Q. Chen, J. Zhang, H. Yan, Modulating polarization rotation to stimulate the high piezocatalytic activity of (K, Na)NbO_3 lead-free piezoelectric materials, Appl. Catal. B Environ. 313 (2022), 121471.
[32] J. He, C. Yu, Y. Hou, X. Su, J. Li, C. Liu, D. Xue, J. Cao, Y. Su, L. Qiao, Accelerated discovery of high-performance piezocatalyst in $BaTiO_3$-based ceramics via machine learning, Nano Energy 97 (2022), 107218.
[33] A.X. Jian Fu, Tianyu Li, Ruzhong Zuo, Ultrahigh piezoelectricity in (Ba,Ca)(Ti,Sn)O_3 lead-free compounds with enormous domain wall contribution, Acta Mater. 230 (2022), 117862.
[34] H. Wang, H. Yuan, Q. Hu, K. Wu, Q. Zheng, D. Lin, Exploring the high-performance (1-x)$BaTiO_3$-x$CaZrO_3$ piezoceramics with multiphase coexistence (R-O-T) from internal lattice distortion and domain features, J. Alloys Compd. 853 (2021), 157167.
[35] Y. Yang, Y. Zhou, J. Ren, Q. Zheng, K.H. Lam, D. Lin, Coexistence of three ferroelectric phases and enhanced piezoelectric properties in $BaTiO_3$–x$CaHfO_3$ lead-free ceramics, J. Eur. Ceram. Soc. 38 (2018) 557–566.
[36] T.T. Panupong Jaiban, Saryrung Khumtrong, Sirintra Lokakaew, Anucha Watcharapasorn, The effects of donor (Nb^{5+}) and acceptor (Cu^{2+}, Zn^{2+}, Mn^{2+}, Mg^{2+}) doping at B-site on crystal structure, microstructure, and electrical properties of $(Ba_{0.85}Ca_{0.15})Zr_{0.1}Ti_{0.9}O_3$ ceramics, J. Alloys Compd. 899 (2022), 162909.
[37] Y. Yang, Y. Zhou, J. Ren, Q. Zheng, K.H. Lam, D. Lin, Phase coexistence and large piezoelectricity in $BaTiO_3$-x$CaSnO_3$ lead-free ceramics, J. Am. Ceram. Soc. 101 (2018) 2594–2605.
[38] J. Wu, D. Xiao, J. Zhu, Potassium–sodium niobate lead-free piezoelectric materials: past, present, and future of phase boundaries, Chem. Rev. 115 (2015) 2559–2595.
[39] V.S. Puli, P. Li, S. Adireddy, D.B. Chrisey, Crystal structure, dielectric, ferroelectric and energy storage properties of La-doped $BaTiO_3$ semiconducting ceramics, Journal of Advanced Dielectrics 5 (2015), 1550027.
[40] Y. Yang, H. Wang, Y. Li, Q. Zheng, J. Liao, W. Jie, D. Lin, Phase coexistence induced strong piezoelectricity in $K_{0.5}Na_{0.5}NbO_3$-based lead-free ceramics, Dalton Trans. 48 (2019) 10676–10682.
[41] J. Gao, Y. Wang, Y. Liu, X. Hu, X. Ke, L. Zhong, Y. He, X. Ren, Enhancing dielectric permittivity for energy-storage devices through tricritical phenomenon, Sci. Rep. 7 (2017) 1–10.
[42] H. Yang, F. Yan, Y. Lin, T. Wang, L. He, F. Wang, A lead free relaxation and high energy storage efficiency ceramics for energy storage applications, J. Alloys Compd. 710 (2017) 436–445.
[43] Y. Chen, L. Yang, D. Zhao, Y. Wang, Q. Zheng, X. He, D. Lin, Enhanced energy storage properties of $Bi_{0.5}Na_{0.5}TiO_3$-based ceramics via regulating the doping content and sintering temperature, Ceram. Int. 49 (2023) 32510–32520.
[44] G. Xue, Q. Wu, G. Li, H. Lin, G. Liu, Y. Chen, X. Liu, Y. Yan, The dielectric and ferroelectric properties of $(Ba_{0.5}Sr_{0.5})TiO_3$-doped $(Bi_{0.5}Na_{0.5})TiO_3$ lead-free ceramics, Journal of Advanced Dielectrics 7 (2017), 1750028.
[45] G. Rossetti Jr., A. Khachaturyan, G. Akcay, Y. Ni, Ferroelectric solid solutions with morphotropic boundaries: vanishing polarization anisotropy, adaptive, polar glass, and two-phase states, J. Appl. Phys. 103 (2008), 114113.
[46] D. Xue, J. Gao, Y. Zhou, X. Ding, J. Sun, T. Lookman, X. Ren, Phase transitions and phase diagram of $Ba(Zr_{0.2}Ti_{0.8})O_3$-x$(Ba_{0.7}Ca_{0.3})TiO_3$ Pb-free system by anelastic measurement, J. Appl. Phys. 117 (2015), 124107.
[47] J. Gao, X. Hu, L. Zhang, F. Li, L. Zhang, Y. Wang, Y. Hao, L. Zhong, X. Ren, Major contributor to the large piezoelectric response in $(1-x)Ba(Zr_{0.2}Ti_{0.8})O_3-x(Ba_{0.7}Ca_{0.3})TiO_3$ ceramics: domain wall motion, Appl. Phys. Lett. 104 (2014), 252909.

[48] H. Fu, R.E. Cohen, Polarization rotation mechanism for ultrahigh electromechanical response in single-crystal piezoelectrics, Nature 403 (2000) 281–283.
[49] D. Damjanovic, A morphotropic phase boundary system based on polarization rotation and polarization extension, Appl. Phys. Lett. 97 (2010), 062906.
[50] M. Acosta, N. Novak, V. Rojas, S. Patel, R. Vaish, J. Koruza, G. Rossetti Jr., J. Rödel, $BaTiO_3$-based piezoelectrics: fundamentals, current status, and perspectives, Appl. Phys. Rev. 4 (2017), 041305.
[51] J.H. Chengye Yu, Mengxi Tan, Yuxuan Hou, Hua Zeng, Chuanbao Liu, Huimin Meng, Yanjing Su, Lijie Qiao, Turab Lookman, Bai Yang, Selective enhancement of photo-piezocatalytic performance in $BaTiO_3$ via heterovalent ion doping, Adv. Funct. Mater. 32 (2022), 2209365.
[52] J. Liao, X. Lv, X.x. Sun, J. Li, H. Wang, Q. Chen, H. Lu, D. Wang, J. Bi, J. Wu, Boosting piezo-catalytic activity of KNN-based materials with phase boundary and defect engineering, Adv. Funct. Mater. (2023), 2303637.